Supplementary Materials

1 Example Input Image Views

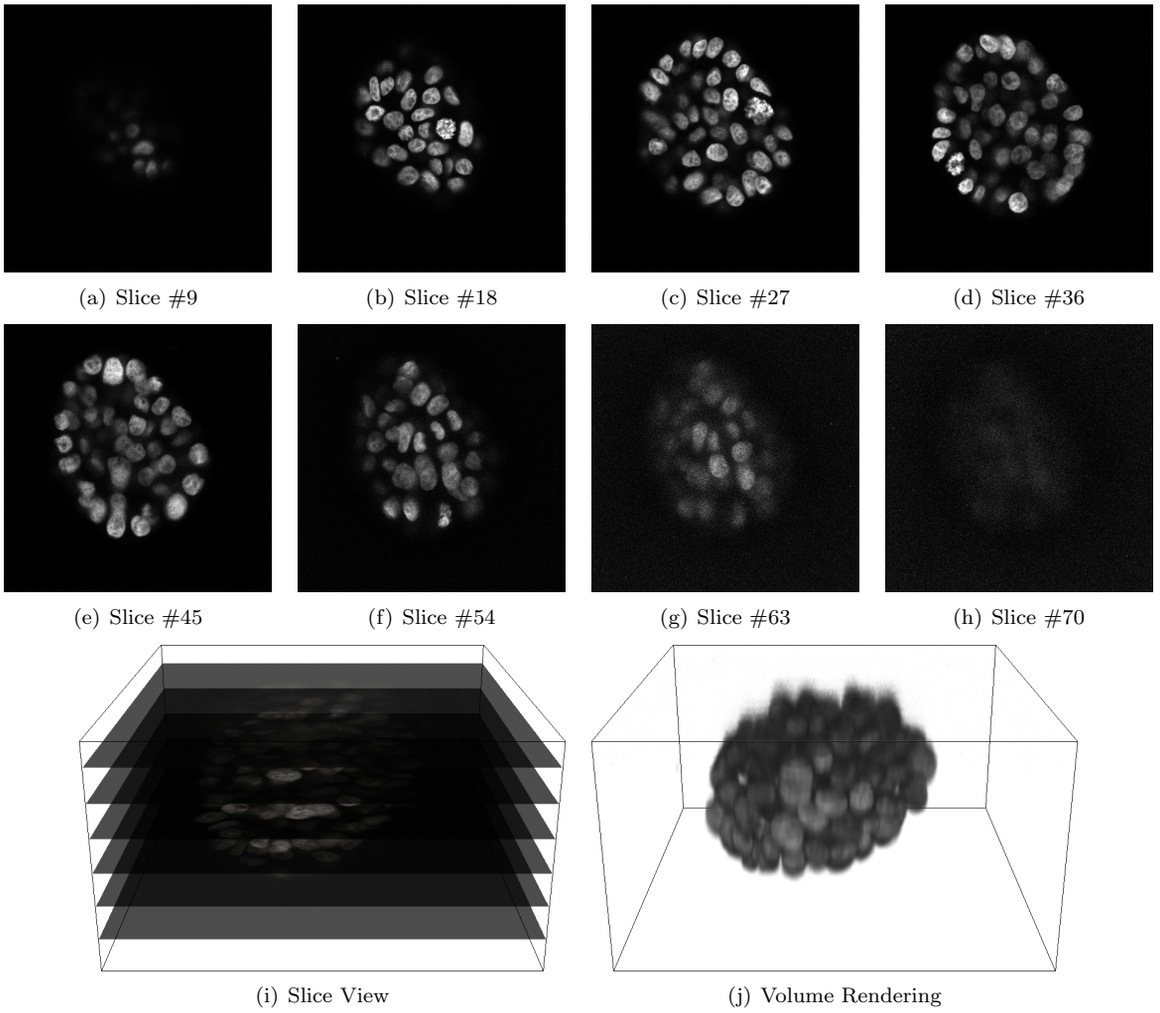

(a) Slice #9 (b) Slice #18 (c) Slice #27 (d) Slice #36

(e) Slice #45 (f) Slice #54 (g) Slice #63 (h) Slice #70

(i) Slice View (j) Volume Rendering

Figure 1: Several slices of a multicellular colony indicating variations in morphometric signature.

2 Harmonic Cut Filtering

Let the linear scale-space representation of image $I_0(x, y, z)$ at scale σ be $I(x, y, z; \sigma) = I_0(x, y, z) * G(x, y, z; \sigma)$ where $G(x, y, z; \sigma)$ is the Gaussian kernel. The calculation of the elliptic features are then given by:

The calculation of the elliptic features are given by:

$$
\begin{aligned}
I_{xx} &= I(x+1, y, z) + I(x-1, y, z) - 2 * I(x, y, z) \\
I_{yy} &= I(x, y+1, z) + I(x, y-1, z) - 2 * I(x, y, z) \\
I_{zz} &= I(x, y, z+1) + I(x, y, z-1) - 2 * I(x, y, z) \\
I_{xy} &= \frac{1}{4} * (I(x+1, y+1, z) + I(x-1, y-1, z) - I(x+1, y-1, z) \\
&\quad - I(x-1, y+1, z)) \\
I_{xz} &= \frac{1}{4} * (I(x+1, y, z+1) + I(x-1, y, z-1) - I(x-1, y, z+1) \\
&\quad - I(x+1, y, z-1)) \\
I_{yz} &= \frac{1}{4} * (I(x, y+1, z+1) + I(x, y-1, z-1) - I(x, y-1, z+1) \\
&\quad - I(x, y+1, z-1)) \\
\det &= I_{xx} * (I_{yy} * I_{zz} - I_{yz} * I_{yz}) - I_{xy} * (I_{xy} * I_{zz} - I_{xz} * I_{yz}) + \\
&\quad I_{xz} * (I_{xy} * I_{yz} - I_{yy} * I_{xz}) \qquad (1) \\
EF &= (I_{xx} * I_{yy} > I_{xy} * I_{xy}) \&\& (I_{xx} * I_{zz} > I_{xz} * I_{xz}) \&\& \\
&\quad (I_{yy} * I_{zz} > I_{yz} * I_{yz}) \qquad (2)
\end{aligned}
$$

A point is considered a bright elliptic feature when EF & $I_{xx} < 0$ & $\det < 0$. Conversely, a point is considered a dark elliptic feature when EF & $I_{xx} > 0$ & $det > 0$. Once the elliptic features are calculated they are interpolated using the harmonic cut filtering. Harmonic cut filtering minimizes the functional:

$$
\frac{1}{2} \iiint_D I_x^2 + I_y^2 + I_z^2 \, dx \, dy \, dz. \qquad (3)
$$

The Euler-Lagrange solution to this optimization is the Laplace equation $\nabla^2 I = I_{xx} + I_{yy} + I_{zz} = 0$ with the Dirchlet boundary condition $I|_{\partial \bar{D}}(x, y, z)$, the restriction of the original image on the boundary of the D's complement $\bar{D} = \Omega - D$ where Ω is the domain of the entire image. The update rule for the image is then given by:

$$
\begin{aligned}
I(i, j, k)^{new} = \frac{1}{6} * (&I^{old}(i-1, j, k) + I^{old}(i+1, j, k) + I^{old}(i, j-1, k) + \\
&I^{old}(i, j+1, k) + I^{old}(i, j, k-1) + I^{old}(i, j, k+1)). \qquad (4)
\end{aligned}
$$

3 Volumetric Curvature Calculation

The Gaussian and the mean curvatures are calculated from the partial derivatives by equation (5) and (6).

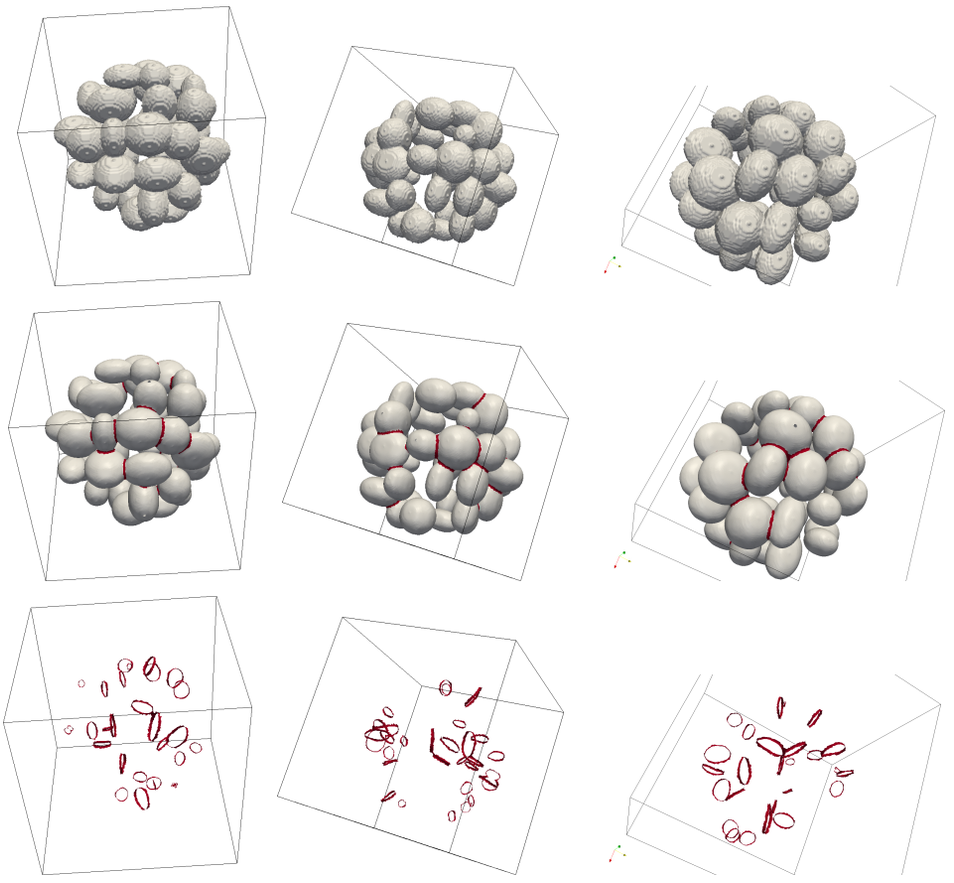

Figure 2: (Best viewed in color.) Three synthetically generated example volumes are depicted in the first row. The corresponding surface models are given in the second row, and the maximum principal curvature is given in the third row. The curvature maxima at the folds where the nuclei overlap is high and can be used for partitioning them.

$$\begin{aligned} K = \frac{1}{h^2}(&I_x^2(I_{yy}I_{zz} - I_{yz}^2) + 2I_yI_z(I_{xz}I_{xy} - I_{xx}I_{yz}) \\ &+ I_y^2(I_{xx}I_{zz} - I_{xz}^2) + 2I_xI_z(I_{yz}I_{xy} - I_{yy}I_{xz}) \\ &+ I_z^2(I_{xx}I_{yy} - I_{xy}^2) + 2I_xI_y(I_{xz}I_{yz} - I_{zz}I_{xy})), \end{aligned} \tag{5}$$

$$\begin{aligned} H = \frac{1}{2h^{3/2}}(&I_x^2(I_{yy} + I_{zz}) + I_y^2(I_{xx} + I_{zz}) + I_z^2(I_{xx} + I_{yy}) \\ &- 2I_yI_zI_{yz} - 2I_xI_zI_{xz} - 2I_xI_yI_{xy}), \end{aligned} \tag{6}$$

where $h = I_x^2 + I_y^2 + I_z^2$. As the Gaussian curvature is the product of the principal curvatures ($K = \kappa_1\kappa_2$), and the mean curvature is given by $H = (\kappa_1 + \kappa_2)/2$, the principal curvatures are calculated by:

$$\kappa = H \pm \sqrt{H^2 - K}. \tag{7}$$

4 Surface Curvature Calculation

Figure 2 depicts the efficacy of the meshing and the surface curvature calculation. First row depicts the segmented raw image (no surface is built), second row is the surface model with surface curvature drawn on it and third row is the surface curvature. There are many ways to create more accurate/fast/simple surface models. However, in our case the simple fast-marching algorithm has been successful (the transition from the first row to the second) and a more accurate but sophisticated model is not necessary. A comparison of the meshing techniques is out of the scope of this paper.

5 Failure Cases

The overall pixel level and object level accuracy of our algorithm is 85% and 96% as presented in the manuscript. Nevertheless, there are cases where the proposed technique is not able to delineate the touching nuclei correctly. Due to the low z-resolution compared to the x-y resolution, two touching nuclei can have accidental alignment and do not form sufficient amount of fold. A 2D visualization of this case is shown in Figure 3, where there is partial strong fold on one side, but none on the other side. In a case like this, depending on the amount of fold, proposed technique might fail to fit a plane if there is not enough support.

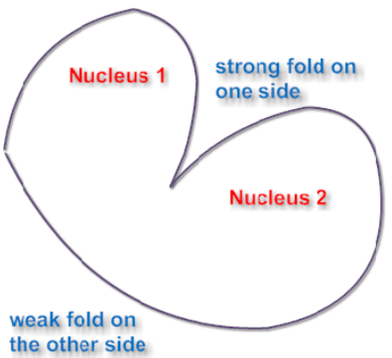

Figure 3: Cancer cell-lines have complex nuclear arrangements. One such arrangement of nuclei that the proposed method could fail is depicted in 2D in this figure. There is strong fold on one side but none on the other side leading to a weak support for plane fitting.

A less common error is introduced as a result of the plane fitting in a colony that is highly packed. In this case, the iterative RANSAC method could fail as it is a greedy algorithm. This behavior could be elevated using a more robust plane fitting algorithm such as the graph-cut based method [1]. Our overall pipeline would be the same in this case with the addition of a different plane fitting algorithm.

References

[1] Hossam Isack and Yuri Boykov. Energy-based geometric multi-model fitting. *International journal of computer vision*, 97(2):123–147, 2012.